

Effect of carbon content on structure and properties of $(\text{CuNiTiNbCr})\text{C}_x\text{N}_y$ high-entropy alloy films

Xin Jiang^a, Pengxiang Zhao^a, Yantao Li^{a,c,*}, Xiaoting Wang^d, Peipei Jing^a, Yongxiang Leng^{a,b,**}

^a Key Laboratory of Advanced Technologies of Materials, Ministry of Education, School of Materials Science and Engineering, Southwest Jiaotong University, Chengdu, 610031, China

^b Sichuan Province International Science and Technology Cooperation Base of Functional Materials, College of Medicine, Southwest Jiaotong University, Chengdu, 610031, China

^c School of Mechanical and Electrical Engineering, Mianyang Teachers' College, Mianyang, 621000, China

^d School of Physical Science and Technology, Southwest Jiaotong University, Chengdu, 610031, China



ARTICLE INFO

Keywords:

High-entropy films
Nanocomposite
Carbonitrides
Tribological properties
Hardness and toughness

ABSTRACT

High-entropy alloy films have shown excellent mechanical performance, but their hardness and wear resistance are still lower than those of conventional hard films such as TiN and CrN, which cannot meet the requirements of hard film applied under severe wear conditions. In this study, the $(\text{CuNiTiNbCr})\text{C}_x\text{N}_y$ high-entropy nanocomposite films were prepared by the double-target co-sputtering method. The effect of carbon content on the film morphology, phase structure, mechanical properties and tribological properties were investigated. With the introduction of carbon atoms in the film, the amorphous/carbonitride/amorphous carbon composite structure is formed. At 21.5 at.% carbon, the film hardness reaches the highest of 18.1 GPa. And at 37.6 at.% carbon, the film shows the highest toughness of $0.96 \text{ MPa m}^{1/2}$ and exhibits the best tribological properties with a low friction coefficient of 0.27 and a wear rate of $1.0 \times 10^{-6} \text{ mm}^3/\text{N}\cdot\text{m}$. The improvement in wear resistance is mainly attributed to the strong toughness of nanocomposite structures and the lubrication effect of amorphous carbon phase. The $(\text{CuNiTiNbCr})\text{C}_x\text{N}_y$ high-entropy nanocomposite films show good application prospect in harsh friction environments.

1. Introduction

With the expansion of the exploration scope of deep space, deep sea and polar regions, mechanical systems must work in extreme environments, such as ultra-low temperature, ultra-high temperature, high load. The traditional ceramic films are easy to fail in high temperature applications due to its brittleness and the thermal expansion coefficient mismatch between ceramic films and the alloy substrate [1,2]. Therefore, solid films with high strength, high toughness, wear resistance, and friction reduction properties are urgently needed.

High-entropy alloy films are a new type of film material designed on the basis of the high-entropy alloy design idea [3], which is composed of five or more metals with nearly equal proportion, and its structure is

generally amorphous or simple solid solution structure phase. High-entropy alloy films have the characteristics of high strength and toughness, low residual stress, wear resistance, radiation resistance, high temperature oxidation resistance and high temperature softening resistance [4–8]. These characteristics make it have potential application value in the field of key parts friction protection.

Researchers have prepared high-entropy alloy films with excellent properties, such as nano-twin CoCrFeNi [9] high-entropy alloy film with high toughness, fine-crystal strengthened CoCrFeNiAl_{0.3} [4] high-entropy alloy film with high hardness, amorphous VAIrTiCrSi [10] high-entropy alloy films with high corrosion resistance, HfNbTaTiZr [11,12] high-entropy alloy films with high biocompatibility. The hardness and wear properties of high entropy alloy films have been improved

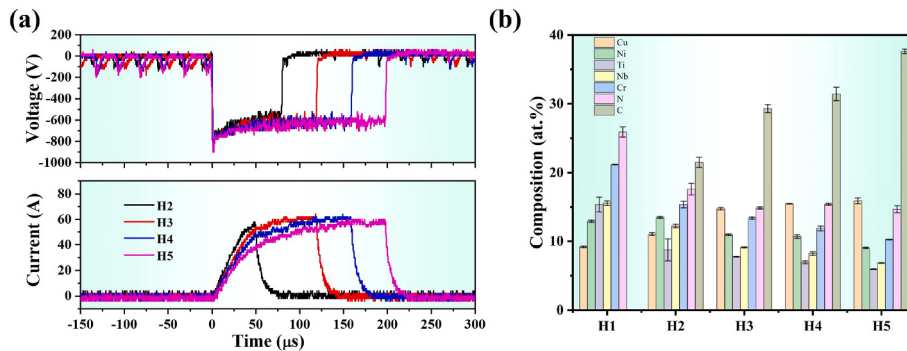
* Corresponding author. Key Laboratory of Advanced Technologies of Materials, Ministry of Education, School of Materials Science and Engineering, Southwest Jiaotong University, Chengdu, 610031, China.

** Corresponding author. Key Laboratory of Advanced Technologies of Materials, Ministry of Education, School of Materials Science and Engineering, Southwest Jiaotong University, Chengdu, 610031, China.

E-mail addresses: liyantao1992@126.com (Y. Li), yxleng@263.net (Y. Leng).

Table 1The deposition parameters of $(\text{CuNiTiNbCr})\text{C}_x\text{N}_y$ films.

Samples	Bias voltage/V	N_2 flow rate/sccm	Power source (Metal)/A	Power source (Graphite)/V- μs-Hz	Graphite target power/W	Deposition pressure/Pa	Deposition time/min
H1	-60	6	2	—	0	0.62	32
H2				800-80-200	245	0.66	
H3				800-120-200	680	0.72	
H4				800-160-200	928	0.74	
H5				800-200-200	1114	0.76	

**Fig. 1.** (a) The HPPMS discharge voltage and current waveforms of graphite target, and (b) the composition of $(\text{CuNiTiNbCr})\text{C}_x\text{N}_y$ HEFs.**Table 2**The configuration entropy of $(\text{CuNiTiNbCr})\text{C}_x\text{N}_y$ films.

Samples	H2-21.5 %	H3-29.3 %	H4-31.4 %	H5-37.6 %
ΔS_{mix}	1.5R	1.85 R	1.82 R	1.74 R

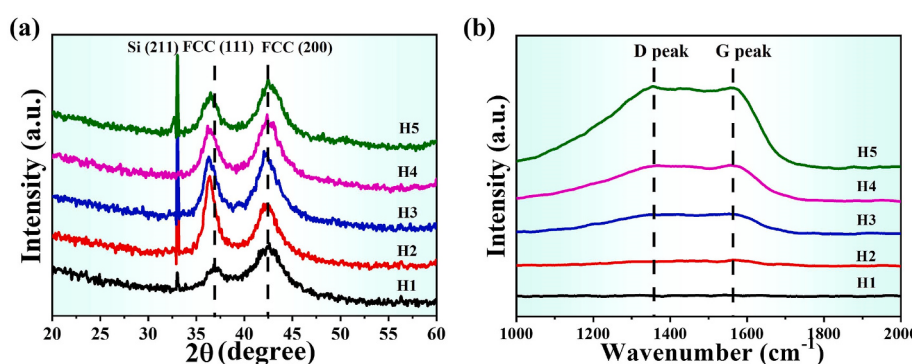
by fine grain strengthening and solid solution strengthening, but they are still lower than that of traditional hard films such as TiN. Generally, the wear rate of nanocrystalline high-entropy alloy films was in the order of $10^{-5} \text{ mm}^3/\text{N}\cdot\text{m}$ [13], which is insufficient to meet the requirements of high load and high frequency wear conditions. Thus, the idea of multi-phase and multi-interface is gradually integrated into the design of high-entropy alloy materials. Some researchers have introduced nitrogen atoms into MoNbTaW high entropy alloy to form alloy/ceramic dual-phase structure, which makes its hardness 4 GPa higher than that of MoNbTaW without nitrogen [14]. Some researchers also introduced carbon and oxygen atoms into CrMoNbWTi to obtain $(\text{Ti},\text{Nb})\text{C}$ and Ti_2O_3 ceramic phase in high entropy alloy, achieving a high hardness of 11.9 GPa [15]. The above results show that incorporating non-metallic elements into high entropy alloy to form alloy/ceramic phase can enhance the hardness of the material. Based on the above reports, the introduction of C, N and other non-metallic atoms into high-entropy alloy films to construct nanocomposite structures has

the potential to improve the strength, toughness and wear resistance of the high-entropy alloy films.

In this paper, based on the principle of dual-phase formation, we selected Ti, Nb and Cr elements that react with C and N to form ceramic phase, Cu and Ni elements that do not react with C and N to form ductile phase, and designed CuNiTiNbCr high-entropy alloy system. Generally, introducing N into films will form Me-N covalent bond ceramic phase, introducing C into films will form Me-C covalent bond ceramic phase, and the introduction of excessive C atoms will make the film form amorphous carbon phase with lubrication [16]. According to literature reports [17,18], nitride has excellent toughness and amorphous carbon

Table 3Raman parameters of $(\text{CuNiTiNbCr})\text{C}_x\text{N}_y$ films with different carbon contents.

Samples	D Peak		G Peak		I_D/I_G
	Position cm^{-1}	FWHM cm^{-1}	Position cm^{-1}	FWHM cm^{-1}	
H1	—	—	—	—	—
H2	1419	222	1576	67	1.03
H3	1376	248	1560	122	1.26
H4	1380	285	1570	119	1.47
H5	1373	285	1565	125	1.45

**Fig. 2.** The (a) XRD and (b) Raman patterns of $(\text{CuNiTiNbCr})\text{C}_x\text{N}_y$ films with different carbon contents.

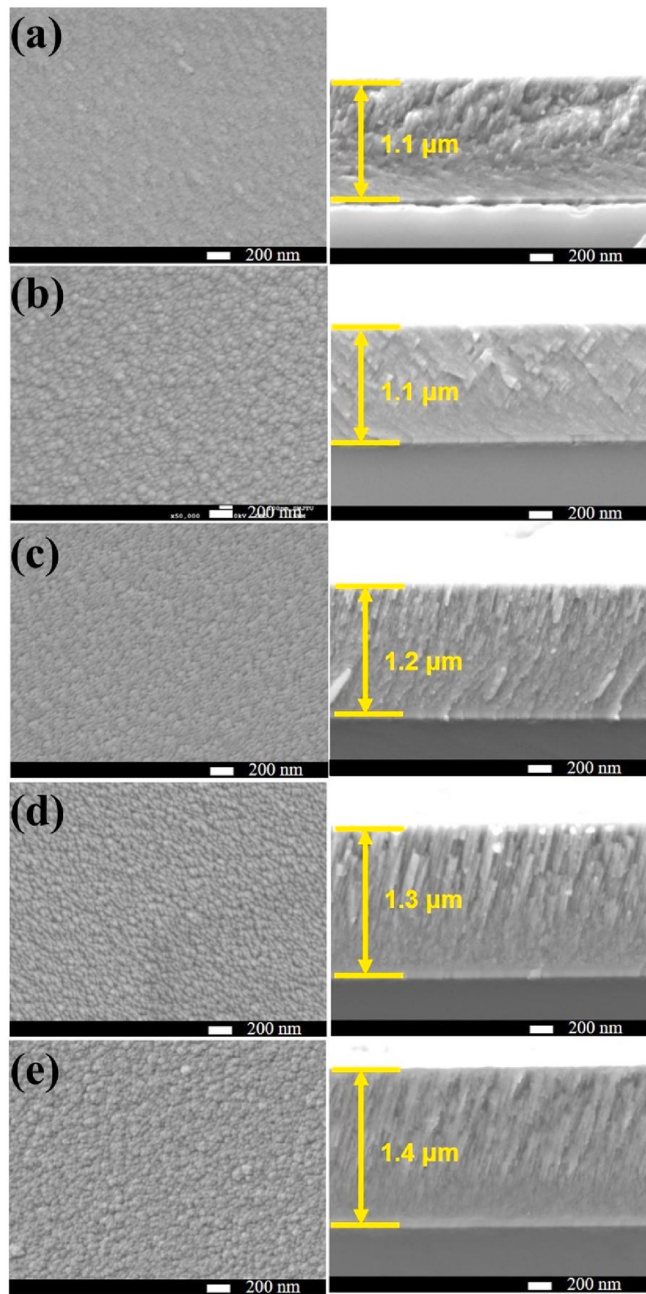


Fig. 3. Surface and cross-sectional morphologies of $(\text{CuNiTiNbCr})_{\text{C}_x\text{N}_y}$ films with different carbon contents (a) H1 (b) H2 (c) H3 (d) H4 (e) H5.

phase can provide lubrication. Therefore, we introduce N and C into film to form Me–N and amorphous carbon phase with lubricating effect. Finally, a nanocomposite structure $(\text{CuNiTiNbCr})\text{CN}$ film with alloy phase, nitride ceramic phase (or carbonitride phase) and amorphous carbon phase are obtained, achieving an improvement in the film strength, toughness and wear resistance. The $(\text{CuNiTiNbCr})_{\text{C}_x\text{N}_y}$ films were prepared on Si and 304 SS substrates by the double-target co-sputtering method with graphite target as carbon source and nitrogen as nitrogen source. The effect of carbon content on the film morphology, and phase structure, mechanical properties and tribological properties are studied.

2. Experimental

In this study, the $(\text{CuNiTiNbCr})_{\text{C}_x\text{N}_y}$ high-entropy nanocomposite

films with different carbon contents were prepared by a double-target co-sputtering method. The CuNiTiNbCr metal splicing target was connected to a direct current (DC) power supply with a constant current of 2A, and the graphite target was connected to a high-power pulsed magnetron sputtering (HPPMS) power supply. The purity of metal target and graphite target was higher than 99.9 %. To control the carbon contents in the films, the HPPMS power supply applied to the graphite target is 0, -800 V-200Hz-80 μs , -800 V-200 Hz-120 μs , -800 V-200 Hz-160 μs and -800 V-200 Hz-200 μs , respectively. During the deposition process, the metal target was pre-sputtered for 2 min to form a 100 nm transition layer, then the graphite target power was turned on and N_2 (6 sccm) was introduced into the vacuum chamber to prepare the $(\text{CuNiTiNbCr})_{\text{C}_x\text{N}_y}$ film, the films deposited at pulse widths of 0, 80, 120, 160, and 200 μs were named H1, H2, H3, H4, and H5, respectively. The relevant deposition parameters are shown in Table 1.

During the film deposition, the target voltage and current waveforms were measured by an oscilloscope (TDS-220, USA) with a Tektronix P-5100 voltage probe and a Pearson 411 current monitor. The composition of the $(\text{CuNiTiNbCr})_{\text{C}_x\text{N}_y}$ films was characterized by an energy dispersive spectrometer (EDS, Oxford, UK). The thickness and cross-sectional morphology of the films were observed using a field emission scanning electron microscope (SEM, JSM-7800F, Japan). The chemical composition and states of the elements in high-entropy films (HEFs) were studied by x-ray photoelectron spectroscopy (XPS, Thermo Scientific K-Alpha, America) using an Al $\text{K}\alpha$ x-ray source (12 kV, 10 mA), and the data were calibrated with $\text{Ar} 2\text{p}_{3/2}$ (241.3 eV). The phase structure of the films was characterized by Cu $\text{K}\alpha$ radiation X-ray diffraction (XRD, Empyrean, Netherlands). The microstructure of $(\text{CuNiTiNbCr})_{\text{C}_x\text{N}_y}$ films was analyzed by transmission electron microscopy (TEM, Jem- 2100f, Japan). The bending morphology of the film was measured by an American XP-2 contact profiler, and the residual stress of the film was calculated by the modified Stoney equation. The hardness was measured by a NANO G200 nanoindenter apparatus with a Berkovich indenter. The nanoindentation test was conducted in CSM mode, with a maximum loading depth of 1000 nm, and the maximum load was related to the film hardness, so the maximum load was different (ranges from 200 mN to 260 mN). There are 6 test points for each sample, and the test spacing was 2 mm. The test was carried out on the surface of films. The data was given in the form of averages/standard deviations. The toughness of the $(\text{CuNiTiNbCr})_{\text{C}_x\text{N}_y}$ films was examined by an indentation test with a Vickers indenter, and the maximum load was 300 g. The relationship between the fracture toughness, K_{IC} , and the length of radial cracks was established [19,20]:

$$K_{IC} = \alpha \left(\frac{E^{\frac{1}{2}}}{H} \right) \frac{P}{C^{\frac{3}{2}}} \quad (1)$$

Where C is the crack length and P is the peak load at indentation, E and H are the elastic modulus and hardness of the film (measured by nano-indentation), where α is the empirical constant, which was related to the geometry of the indenter ($\alpha = 0.016$ for the Vickers indenters). By using the ball-disk reciprocating friction method (Swiss CSEM) at a relative humidity of roughly 55 % RH and a temperature of 12 ± 1 °C, the wear characteristics of $(\text{CuNiTiNbCr})_{\text{C}_x\text{N}_y}$ films were assessed. Using a normal load of 2 N, a velocity of 12 mm/s, an amplitude of 6 mm, and a sliding time of 5000 s, all tribological tests were conducted. A tungsten carbide ball with the diameter of 6 mm was used as the tribological counterpart. The wear track profile of the film was measured by a stylus profiler (XP-2, USA). The wear trajectory and its morphology were observed by field emission scanning electron microscopy (SEM, JSM-7800F, Japan). The wear rate of the film was calculated by $\mu = \frac{V}{LS}$, where μ , V , L and S represent the wear rate, wear volume, load and sliding distance, respectively.

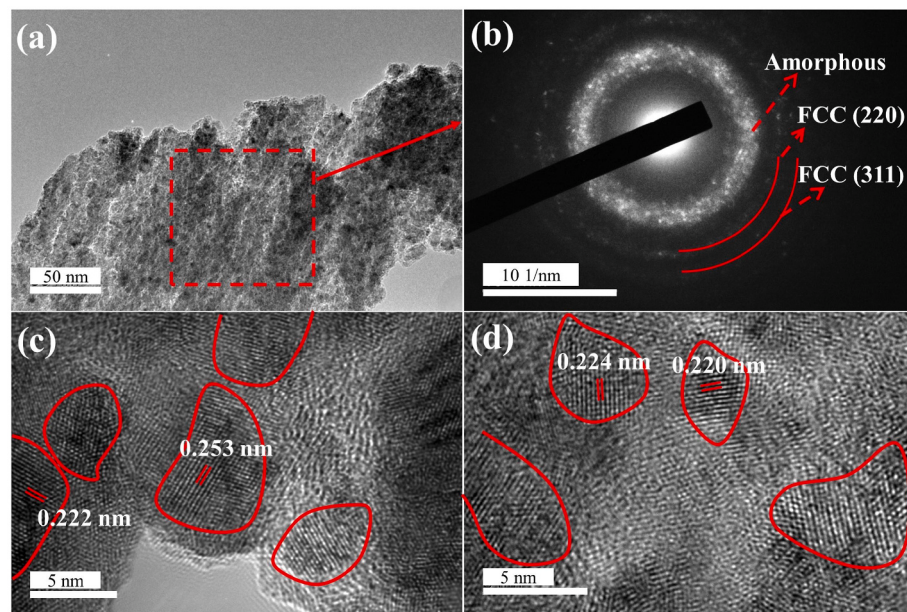


Fig. 4. TEM images of H5 sample: (a) low magnification TEM image; (b) selected area electron diffraction pattern; (c) and (d) high resolution TEM image.

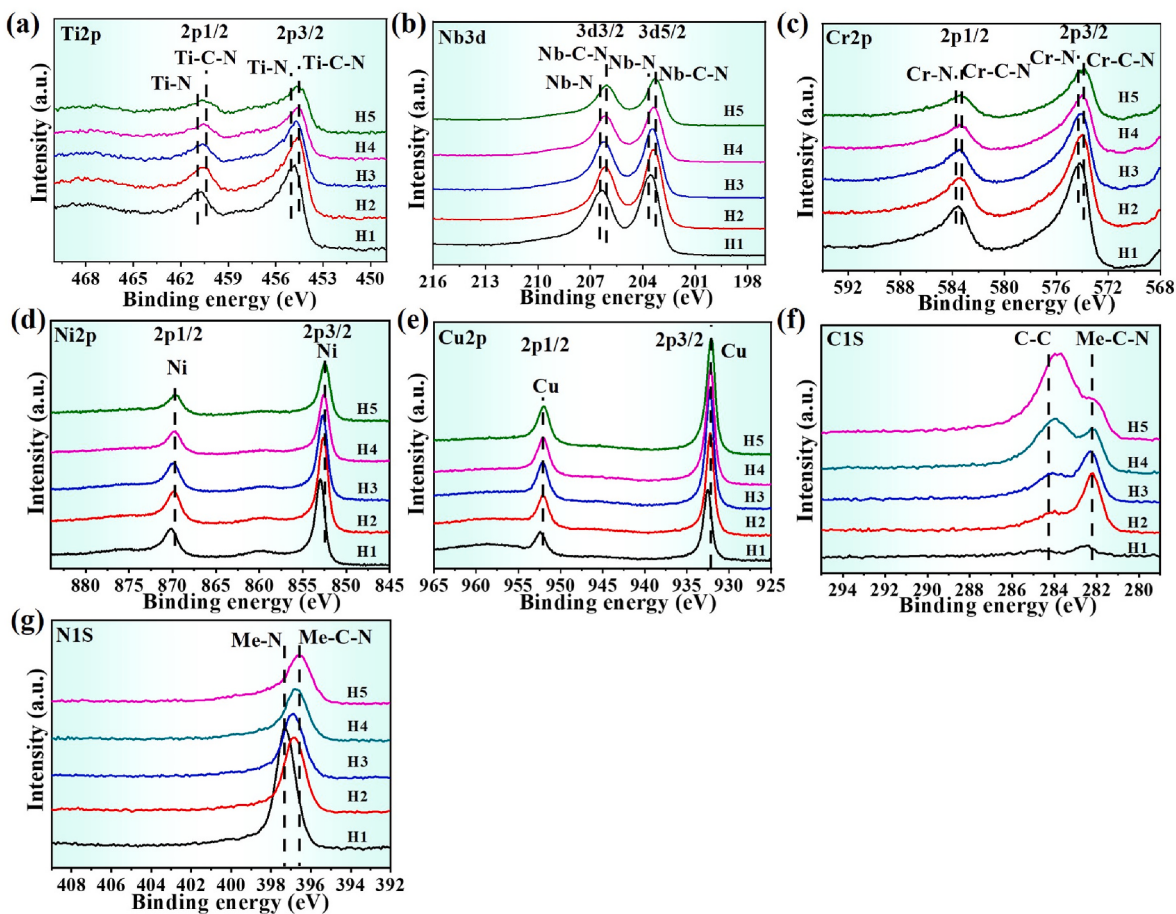


Fig. 5. XPS high resolution spectra of elements in $(\text{CuNiTiNbCr})_{\text{x}}\text{N}_{\text{y}}$ films with different carbon contents (a) Ti2p, (b) Nd3d, (c) Cr2p, (d) Ni2p, (e) Cu2p, (f) C1s and (g) N1s.

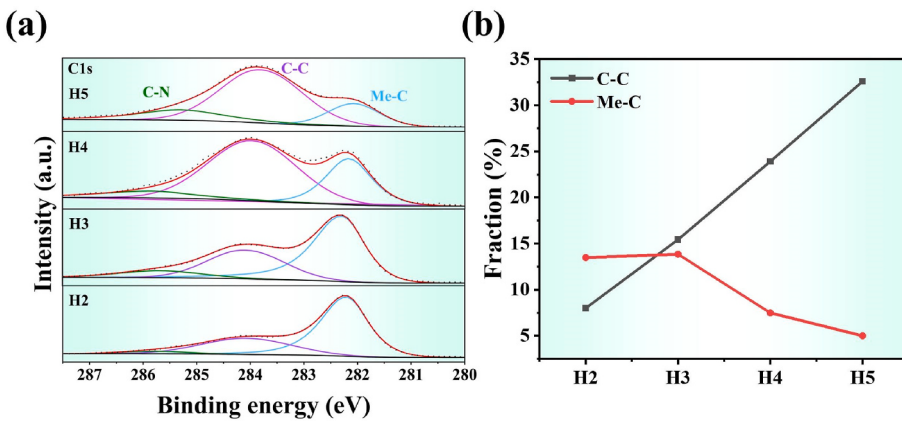


Fig. 6. (a) XPS C1s fitting spectrum, (b) Proportion of C–C bond and Me–C bond in the $(\text{CuNiTiNbCr})\text{C}_x\text{N}_y$ films.

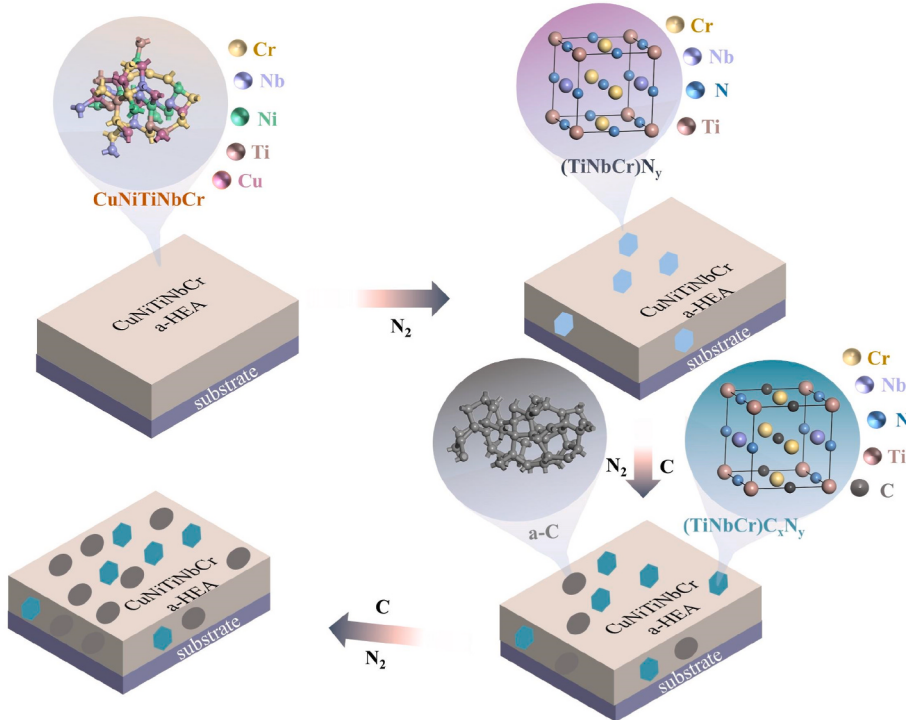


Fig. 7. Schematic diagram of structural evolution of $(\text{CuNiTiNbCr})\text{C}_x\text{N}_y$ HEFs with different carbon and nitrogen contents.

3. Results and discussion

3.1. HPPMS plasma discharge and film composition

In this study, the carbon contents in the films are controlled by varying the discharge pulse width of the graphite target, and the discharge voltage and current curves of the graphite target are shown in **Fig. 1a**. It is observed that after the voltage reaches -800 V, the voltage gradually decreases to a plateau value of -600 V, which is because the current limiting resistor divides part of the voltage. The peak current of the graphite target does not increase with the pulse width, which indicates that the peak power of HPPMS is similar. The average power of the graphite target is calculated to be 0 W, 245 W, 680 W, 928 W and 1114 W for the pulse widths of 0 , 8 μs , 120 μs , 160 μs and 200 μs , respectively.

Fig. 1b shows the results of the composition of $(\text{CuNiTiNbCr})\text{C}_x\text{N}_y$ films deposited at different graphite target powers, from which it can be learned that the composition of the five metal elements ranges from 5 at.

% to 35 at.%. The content of N is in the range of 14.6 at.% ~ 25.9 at.%. With the increase of graphite target power, the carbon content in the films gradually increase, and the carbon contents in H1 \sim H5 are 0 , 21.5 at.%, 29.3 at.%, 31.4 at.%, and 37.6 at.%, respectively, which indicate that the $(\text{CuNiTiNbCr})\text{C}_x\text{N}_y$ films with different carbon contents are successfully prepared. The contents of the N, Ni, Ti, Nb, and Cr gradually decrease with the increase of carbon content. The proportion of Cu elements increases with the increase of carbon, which may be related to target “poisoning”. Because Ti, Nb, and Cr react with N to form a nitride layer on the surface of target, which reduces its sputtering rate and leads to an increase in the relative content of Cu. **Table 2** shows the mixing entropy of high entropy alloy films with different carbon content. With the development of high-entropy alloys, researchers pay more attention to the properties of high-entropy alloys, and relax the restrictions on the range of elements and configuration entropy. The definition has evolved into the well-accepted requirement of a system based on four or more elements each constituting $5\text{--}35$ at.% with a microstructure containing at least one random solid solution phase or amorphous phase [21,22].

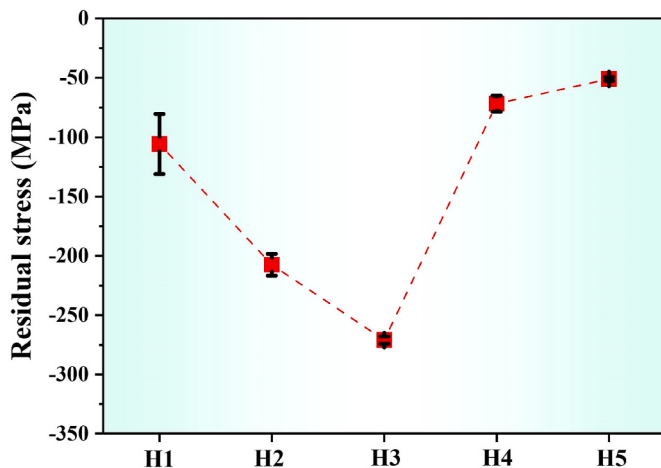


Fig. 8. The residual stress of $(\text{CuNiTiNbCr})\text{C}_x\text{N}_y$ films with different carbon contents.

Fig. 2a shows the XRD patterns of the $(\text{CuNiTiNbCr})\text{C}_x\text{N}_y$ films with different carbon contents. All samples show three peaks and the peak positions are around 33.0° , 36.8° , and 42.4° , respectively. By comparison with the standard diffraction cards, it can be observed that the sharp diffraction peak at 2θ of 33.0° corresponds to the (211) crystal plane of

the Si substrate. The other two wide diffraction peaks are related to the structure of the film and correspond to the FCC(111) and FCC(200) crystal plane diffraction peaks. With the introduction of carbon atoms into the film, the diffraction peaks of H2, H3, H4, and H5 all shift to lower diffraction angles, which may be related to the formation of the carbon nitriding phase caused by carbon atoms entering the FCC nitride ceramic phase. By refining the diffraction peaks of the (111) and (200) crystal planes, the grain sizes of nanocrystals in the film are obtained. The grain sizes of H1, H2, H3, H4, and H5 samples obtained from Scheler's formula are 8.7, 6.8, 6.7, 5.3, and 4.6 nm, respectively, which indicates that the crystal size of the film decreases with the introduction of carbon atoms. The Raman spectra in Fig. 2b show two patterns, namely, the D peak at 1350 cm^{-1} and the G peak at 1550 cm^{-1} . With the increase of C doping in the film, the intensity of D and G peaks in the Raman spectra are gradually enhanced. After calculating the I_D/I_G ratio, it is obtained that the I_D/I_G of H2 sample is 1.03, H3 sample is 1.26, H4

Table 4

The crack length and fracture toughness (K_{IC}) of the $(\text{CuNiTiNbCr})\text{C}_x\text{N}_y$ films.

Samples	Crack length (μm)	K_{IC} ($\text{MPa}\cdot\text{m}^{1/2}$)
H1	37.7 ± 3.2	0.76 ± 0.10
H2	35.6 ± 0.9	0.81 ± 0.03
H3	33.5 ± 0.5	0.94 ± 0.02
H4	34.2 ± 0.8	0.92 ± 0.03
H5	32.0 ± 1.1	0.96 ± 0.05

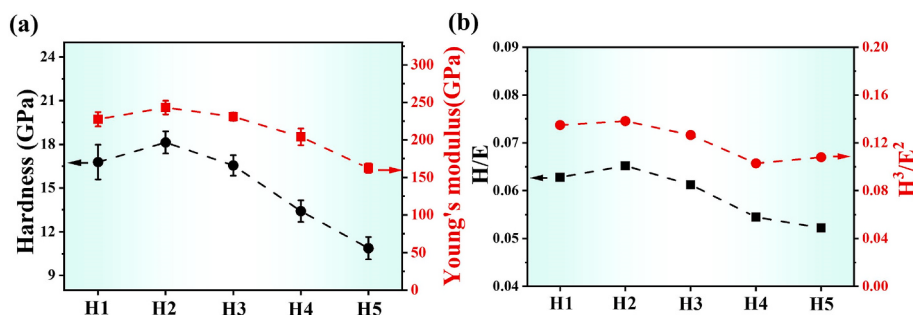


Fig. 9. (a) The hardness and modulus and (b) the calculated H^3/E^2 , H/E values of $(\text{CuNiTiNbCr})\text{C}_x\text{N}_y$ films deposited at different graphite target powers.

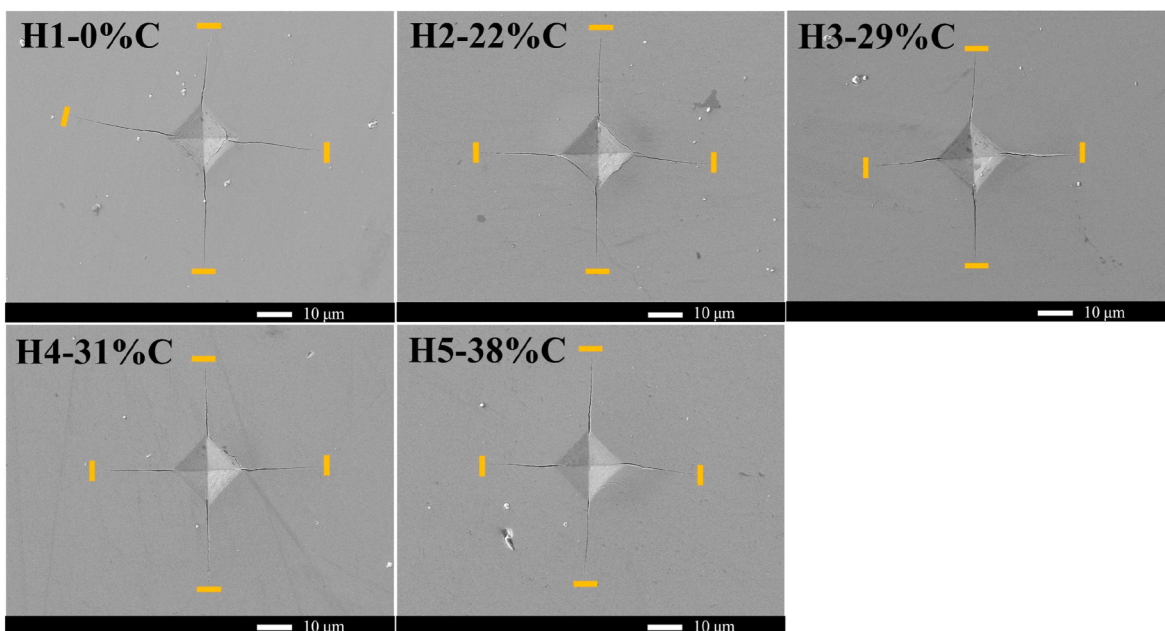


Fig. 10. Vickers indentation morphology of the $(\text{CuNiTiNbCr})\text{C}_x\text{N}_y$ films with different carbon contents.

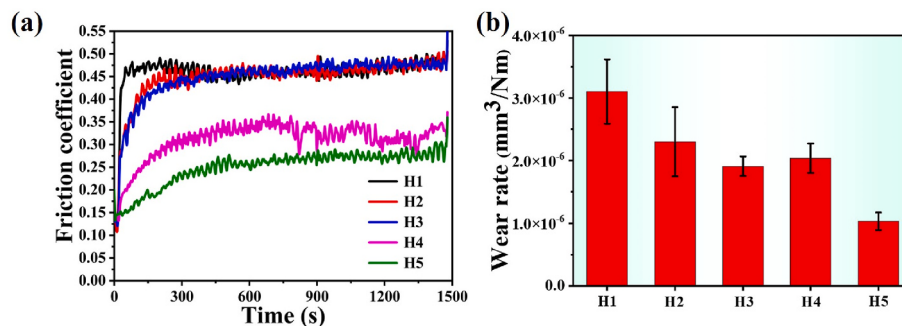


Fig. 11. (a) Friction coefficient and (b) wear rate of $(\text{CuNiTiNbCr})_{\text{x}}\text{N}_{\text{y}}$ films with different carbon contents.

sample is 1.47 and H5 sample is 1.45 as shown in Table 3. The sp^2 content of H2–H5 films increases with the increase of carbon content. The results show that the amorphous carbon structure is graphitized and the bonding state gradually changes from sp^3 hybrid to sp^2 hybrid.

3.2. Microstructure and elements chemical states of the HEFs

Fig. 3 shows the surface and cross-sectional morphology of the $(\text{CuNiTiNbCr})_{\text{x}}\text{N}_{\text{y}}$ films. All samples show uneven granular bumps surface and the cross-sectional morphology of films are obvious differences at different carbon contents. The H1 samples showing obvious columnar structures, while H2 sample shows denser non-columnar structures, and H3 sample shows finer columnar structures. With the further increase in carbon content, the columnar structure size of H4 sample increases slightly, and the H5 sample has a denser columnar structure.

Fig. 4 shows the TEM images of the H5 sample. The low magnification images (Fig. 4a) reveal a clear contrast between light and dark areas, indicating the possible presence of different phases within the film. From the high-resolution TEM images (Fig. 4c and d), it can be seen that a large number of nanocrystals about 5 nm in size are wrapped by bright amorphous regions, which indicates the coexistence of amorphous and nanocrystalline structures in the film. The grain size observed by TEM is basically consistent with that obtained from XRD results. The nanocrystalline region has a dark contrast due to the larger atomic mass of the metal, while the amorphous region contains a large number of carbon atoms, and the lower atomic mass of carbon results in a bright contrast. Fig. 4b displays the SAED pattern, which includes a broad amorphous ring in the center and diffraction rings corresponding to the FCC (220) and (311) crystal planes. These results are in agreement with the XRD findings. The FCC (111) and (200) diffraction peaks shown in the XRD patterns are not observed in the SAED, which may be because their positions overlap with the amorphous rings. The nanocrystals in the high-resolution images are measured at a crystal plane spacing of 0.25 nm and 0.22 nm, which correspond to the (111) and (200) crystal planes of the FCC phase, respectively. The above results show that the $(\text{CuNiTiNbCr})_{\text{x}}\text{N}_{\text{y}}$ films consist of amorphous and crystalline dual-phase structures.

The chemical states of the elements in the $(\text{CuNiTiNbCr})_{\text{x}}\text{N}_{\text{y}}$ films are characterized by XPS. The chemical states of the five metallic elements as well as carbon and nitrogen are analyzed based on the NIST XPS database and literature reports [23–27], and the results are shown in Fig. 5. From the Ti2p high-resolution spectrum (Fig. 5a) of the H1 sample, it is clear that the Ti is mainly present in the form of $\text{Ti}-\text{N}$. And the H1 sample was oxidized during preservation, and an oxide layer appeared on the sample surface. Cu and Ni atoms form the strong chemical bonds with oxygen atoms, resulting in the change of electron energy level. The binding energy of Cu and Ni ion shift towards high energy, resulting a peak shift to the left. With the introduction of carbon, the Ti2p peak shifts towards the low binding energy. The binding energy of $\text{Ti}-\text{C}$ is significantly lower than that of $\text{Ti}-\text{N}$ [28]. Therefore, it

is speculated that, as the carbon content increases, C atoms enter the $\text{Ti}-\text{N}$ lattice to form $\text{Ti}-(\text{C},\text{N})$, and the binding energy of $\text{Ti}-(\text{C},\text{N})$ is lower than that of $\text{Ti}-\text{N}$. Similar to the Ti, as the carbon content increases, both the Nb 3d peak (Fig. 5b) and the Cr 2p peak (Fig. 5c) shift toward the lower binding energy, indicating that Nb and Cr react with C to form $\text{Nb}-(\text{C},\text{N})$ and $\text{Cr}-(\text{C},\text{N})$. The Cu 2p (Fig. 5e) and Ni 2p (Fig. 5d) peaks do not shift with the introduction of C, and both Cu and Ni exist in metallic state. From the high resolution spectrum of C1s (Fig. 5f), it can be seen that with the increase of carbon content in the film, the metal carbonitride phase ($\text{Me}-(\text{C},\text{N})$) dominates in H2, and then with the further increase of carbon content, the amorphous carbon ($\text{C}-\text{C}$) peak dominates in H4 and H5. The N 1s high resolution spectra (Fig. 5g) shows that with the introduction of carbon atoms, the binding energy corresponding to $\text{Me}-\text{N}$ in the film shifted to a lower binding energy, which also confirmed that the C atom entered the nitrides phase to form $\text{Me}-(\text{C},\text{N})$.

In order to analyze the ratio of metal carbide phase and amorphous carbon phase, we performed a split-peak fit to the C1s peak, and the results are shown in Fig. 6a. The two peaks obtained from the fit represent the $\text{C}-\text{C}$ bond (including $\text{C}-\text{C}$ sp^3 and $\text{C}=\text{C}$ sp^2) and the $\text{Me}-\text{C}$ bond, respectively. The proportional change of the two phases is further obtained by calculating the peak area, as shown in Fig. 6b, which are calculated by $A_{\text{C-C}}/(A_{\text{C-C}} + A_{\text{Me-C}}) \times R_{\text{C}}$ and $A_{\text{Me-C}}/(A_{\text{C-C}} + A_{\text{Me-C}}) \times R_{\text{C}}$. $A_{\text{C-C}}$ and $A_{\text{Me-C}}$ are the fitted peak areas of $\text{C}-\text{C}$ and $\text{Me}-\text{C}$ in Fig. 6a, and R_{C} is the proportion of carbon atoms. After the introduction of the C in the film, the carbonitride phase and a-C phase are formed in the film. With the increase of carbon content, the carbonitride phase firstly increases and then decreases, while the amorphous carbon phase gradually increased and began to dominate in H4. The proportion of $\text{C}-\text{C}$ rapidly increases from 8.0 % in H2 film to 32.6 % in H5 film. Fig. 7 shows the evolution process of the film structure with the introduction of N and C atoms. Firstly, the introduced N atoms react with Ti, Nb and Cr to form a dual phase structure of amorphous and nitride phases. Then, the introduced carbon atoms will combine with Ti, Nb, Cr and N to form $(\text{TiNbCr})\text{NC}$ ceramic phase. As the carbon content increases, excess carbon precipitates to form amorphous carbon phase. Finally, as the carbon content further increases, amorphous carbon phase dominates in the $(\text{CuNiTiNbCr})_{\text{x}}\text{N}_{\text{y}}$ HEFs.

3.3. Mechanical properties

Fig. 8 shows that all $(\text{CuNiTiNbCr})_{\text{x}}\text{N}_{\text{y}}$ films exhibit the compressive stress. With the increase of the carbon contents, the compressive stress of the $(\text{CuNiTiNbCr})_{\text{x}}\text{N}_{\text{y}}$ films increase from 105 MPa (H1) to 270 MPa (H3), and then decrease to 71 MPa (H4) and 50 MPa (H5). The variation of stress in $(\text{CuNiTiNbCr})_{\text{x}}\text{N}_{\text{y}}$ films is related to their microstructure. As the graphite target power increases, a significant amount of carbon combines with metal and nitrogen to form the carbonitride ceramic phase in the film. The structure formed by numerous strong covalent bonds generates large compressive stress in the film. As the carbon content continues to increase, the carbon atoms in the metal carbonitride phase reach saturation. The excess carbon then forms an

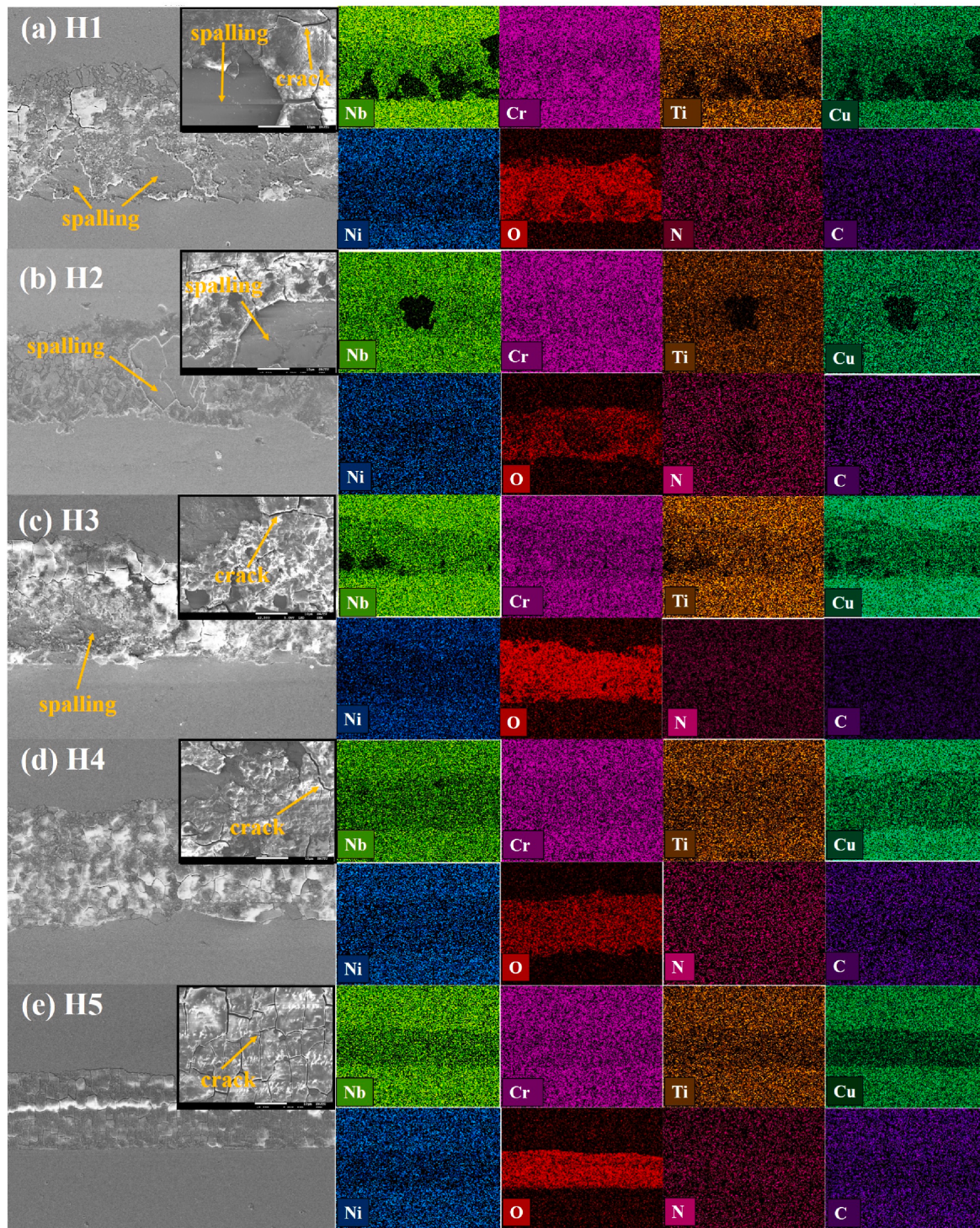


Fig. 12. Wear track morphologies and composition distribution of $(\text{CuNiTiNbCr})_{\text{C}}\text{xN}_{\text{y}}$ films deposited at different graphite target powers (a) H1, (b) H2, (c) H3, (d) H4, (e) H5.

amorphous carbon phase, which has a relatively loose structure and leads to stress relaxation, resulting in a reduction of stress in the film.

Fig. 9 presents the hardness and elastic modulus of $(\text{CuNiTiNbCr})_{\text{C}}\text{xN}_{\text{y}}$ films, along with their H/E and H^3/E^2 values. The H/E stands the elastic strain to failure capability of the films [29]. And the H^3/E^2 stands film's resistance to plastic deformation [30]. Fig. 9a demonstrates that, as the carbon content increases, the hardness and Young's modulus of the films initially increase and then decrease. The H2 sample exhibits the highest hardness and modulus, measuring 18.1 GPa and 243 GPa,

respectively. The change in hardness and modulus of the film is closely related to the phase structure of the film. A low carbon content results in the formation of a significant amount of carbonitride phase, which increases the film's hardness. With the increase of carbon, the precipitation of a large amount of amorphous carbon phase subsequently decreases the film's hardness. This phenomenon has been reported in $\text{TiC}/\text{a-C}$, $\text{CrC}/\text{a-C}$ and other nano-composite films [31–33]. From H/E and H^3/E^2 results, the H2 sample shows the best toughness. In order to test the toughness of the film more accurately, the indentation method is

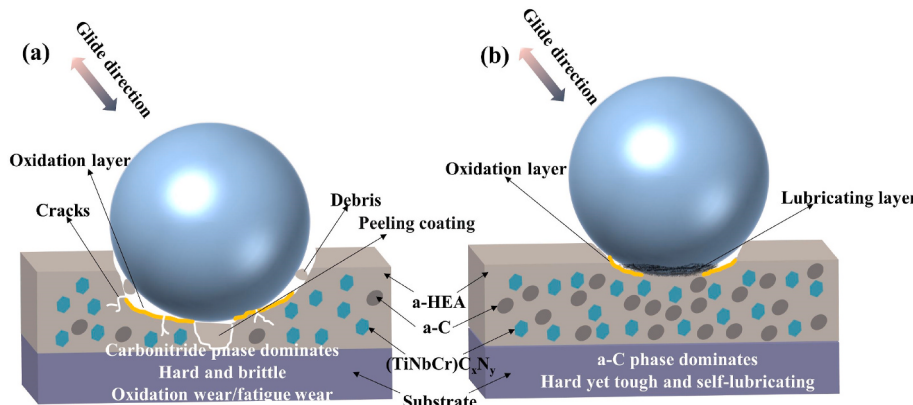


Fig. 13. Schematic diagram of wear mechanism of $(\text{CuNiTiNbCr})\text{C}_x\text{N}_y$ films with (a) low carbon content and (b) high carbon content.

used to evaluate the fracture toughness (K_{IC}) of the $(\text{CuNiTiNbCr})\text{C}_x\text{N}_y$ films.

The Vickers indentation fracture patterns of the $(\text{CuNiTiNbCr})\text{C}_x\text{N}_y$ films are shown in Fig. 10. The radial crack lengths and the fracture toughness (K_{IC}) calculated according to equation are given in Table 4. As the carbon content increases, the fracture toughness of H3, H4, and H5 samples gradually increases. The fracture toughness of the H3, H4, and H5 samples is $0.94 \pm 0.02 \text{ MPa m}^{1/2}$, $0.92 \pm 0.03 \text{ MPa m}^{1/2}$ and $0.96 \pm 0.05 \text{ MPa m}^{1/2}$, respectively. It can be seen that the fracture toughness value of $(\text{CuNiTiNbCr})\text{C}_x\text{N}_y$ films is inconsistent with the variation trend of H/E and H^3/E^2 . This result indicates the limitations of using H/E and H^3/E^2 to characterize the toughness of films. The increase in film toughness is related to the large amount of phase interface formed after the introduction of the carbonitride phase and amorphous carbon phase. The crack deflection and splitting occurred at the phase interface, and the stress intensity at the crack tip is reduced, resulting in the inhibition of crack spreading and the increase in film toughness.

3.4. Tribological properties

Fig. 11a shows the friction coefficient curves of $(\text{CuNiTiNbCr})\text{C}_x\text{N}_y$ films deposited at different graphite target power. The friction coefficients of the H1, H2, and H3 samples are very close, about 0.48. And with the increase in carbon content, the friction coefficients of H4 and H5 decrease to 0.35 and 0.27, respectively. The reduction of the friction coefficient is mainly related to the formation of a large amount of amorphous carbon phases with lubricating effect. Fig. 11b shows that the wear rate of $(\text{CuNiTiNbCr})\text{C}_x\text{N}_y$ films. With the increase of carbon content, the wear rate gradually decreases from $3.1 \times 10^{-6} \text{ mm}^3/\text{N}\cdot\text{m}$ (H1) to $1.0 \times 10^{-6} \text{ mm}^3/\text{N}\cdot\text{m}$ (H5). The reduction in wear rate is mainly attributed to the lubricating effect of the large amount of amorphous carbon phase in the film and the improvement in toughness of the film originating from the nanocomposite structure. In summary, the H5 sample exhibits the most excellent tribological properties with the lowest friction coefficient and wear rate.

In order to analyze the wear mechanism, the wear track morphology and composition of $(\text{CuNiTiNbCr})\text{C}_x\text{N}_y$ films are investigated by SEM and EDS. As shown in Fig. 12, the wear tracks of H1, H2 and H3 show obvious pits and spalling, and the wear tracks of H4 and H5 present a lot of cracks, which are typical features of fatigue wear [34,35]. It is worth noting that the wear tracks of H4 and H5 exhibit only crack formation without film spalling. This phenomenon can be attributed to the increased toughness resulting from the elevated carbon content. The good toughness improves the film's resistance to fatigue-induced spalling. Furthermore, chemical composition analysis of the worn surfaces reveals a substantial presence of oxygen element within the wear tracks. This finding indicates that due to the considerable heat generated during the friction and deformation processes, oxidation occurs on the worn

surface, providing evidence for the existence of oxidation wear [36,37]. The homogeneous and complete oxide layer can prevent direct contact between the film and the grinding ball and improve the wear resistance of the film. The oxide layer and the film in H1, H2 and H3 have obvious local spalling, which might be one of the reasons for their high wear rate. The principle of wear mechanisms is illustrated in Fig. 13. When the carbon content is low, the film is primarily composed of a high-entropy alloy phase and carbonitride phase. During the friction process, air contact with the film surface, forming an oxide layer that effectively isolates direct contact between the film and grinding ball, thereby enhancing the wear resistance of the film. However, due to the poor toughness of the low-carbon content film, the oxide layer and the film are prone to fatigue peeling during friction, resulting in an elevated wear rate, as depicted in Fig. 13a. As the carbon content increases, a large amount of amorphous carbon phase precipitates within the film. On one hand, this phenomenon augments the number of phase interfaces within the film, thereby elevating its resistance to crack propagation and effectively inhibiting fatigue peeling. On the other hand, the amorphous carbon phase within the film serves as a lubricant, transferring to the surface of the friction counterpart to form a lubricating layer during the friction process. This substantially reduces the friction coefficient of the film and significantly enhances its wear resistance, as illustrated in Fig. 13b.

4. Conclusion

We have used nitrogen as the nitrogen source and graphite target as the carbon source, and deposited $(\text{CuNiTiNbCr})\text{C}_x\text{N}_y$ high-entropy alloys/carbonitride/amorphous carbon nanocomposite films by double-target co-sputtering technique. As the carbon content increases, the carbon atoms first combine with Ti, Nb, Cr and N to form the carbonitride phase. When the carbon in the carbonitride phase reaches saturation (carbon content exceeds 29.3 at.%), the amorphous carbon phase begins to precipitate, ultimately dominating the high-entropy film. At a carbon content of 21.5 at.%, a large number of carbonitride ceramic phases formed in the film, resulting in the highest hardness and modulus of 18.1 GPa and 243 GPa, respectively. At 37.6 at.% carbon content, the films show the best fracture toughness and tribological properties. The friction coefficient of the films at this composition was as low as 0.27, with a wear rate of $1.0 \times 10^{-6} \text{ mm}^3/\text{N}\cdot\text{m}$. The excellent wear resistance of the film can be attributed to its good toughness and lubricating effect of the amorphous carbon phase. This work provides an effective strategy for designing and preparing novel high-entropy nanocomposite protective films suitable for harsh friction conditions.

Declaration of competing interest

No competing financial interests or personal relationships that could

have appeared to influence the work reported in this paper, and the manuscript is approved by all authors for publication. I would like to declare on behalf of my co-authors that the work described was original research that has not been published previously, and not under consideration for publication elsewhere, in whole or in part.

Acknowledgment

This work was supported by the National Natural Science Foundation of China (Grant Nos. 51975564 and 52375206), the Sichuan Science and Technology Project (Grant No. 2021YFSY0050), the State Key Laboratory of Acoustics, Chinese Academy of Sciences (SKLA202214) and the Fundamental Research Funds for the Central Universities (No. 2682021CX103).

References

- [1] L.S. Qiu, X.D. Zhu, S. Lu, G.Y. He, K.W. Xu, Quantitative evaluation of bonding strength for hard coatings by interfacial fatigue strength under cyclic indentation, *Surf. Coat. Technol.* 315 (2017) 303–313, <https://doi.org/10.1016/j.surfcoat.2017.02.045>.
- [2] K. Sarakinos, J. Alami, S. Konstantinidis, High power pulsed magnetron sputtering: a review on scientific and engineering state of the art, *Surf. Coat. Technol.* 204 (11) (2010) 1661–1684, <https://doi.org/10.1016/j.surfcoat.2009.11.013>.
- [3] W. Li, P. Liu, P.K. Liaw, Microstructures and properties of high-entropy alloy films and coatings: a review, *Mater. Res. Lett.* 6 (4) (2018) 199–229, <https://doi.org/10.1080/21663831.2018.1434248>.
- [4] W. Liao, S. Lan, L. Gao, H. Zhang, S. Xu, J. Song, X. Wang, Y. Lu, Nanocrystalline high-entropy alloy (CoCrFeNiAl0.3) thin-film coating by magnetron sputtering, *Thin Solid Films* 638 (2017) 383–388, <https://doi.org/10.1016/j.tsf.2017.08.006>.
- [5] X.B. Feng, J.Y. Zhang, Y.Q. Wang, Z.Q. Hou, K. Wu, G. Liu, J. Sun, Size effects on the mechanical properties of nanocrystalline NbMoTaW refractory high entropy alloy thin films, *Int. J. Plast.* 95 (2017) 264–277, <https://doi.org/10.1016/j.ijplas.2017.04.013>.
- [6] S. Zheng, Z. Cai, J. Pu, C. Zeng, S. Chen, R. Chen, L. Wang, A feasible method for the fabrication of VAI TiCrSi amorphous high entropy alloy film with outstanding anti-corrosion property, *Appl. Surf. Sci.* 483 (2019) 870–874, <https://doi.org/10.1016/j.apsusc.2019.03.338>.
- [7] A.D. Pogrebnyak, I.V. Yakushchenko, O.V. Bondar, V.M. Beresnev, C. Kozak, Irradiation resistance, microstructure and mechanical properties of nanostructured (TiZrHfVNbTa)N coatings, *J. Alloys Compd.* 679 (2016) 155–163, <https://doi.org/10.1016/j.jallcom.2016.04.064>.
- [8] K.D. Yu, W. Zhao, Z. Li, N. Guo, G.C. Xiao, H. Zhang, High-temperature oxidation behavior and corrosion resistance of in-situ TiC and Mo reinforced AlCoCrFeNi-based high entropy alloy coatings by laser cladding, *Ceram. Int.* 49 (6) (2023) 10151–10164, <https://doi.org/10.1016/j.ceramint.2022.11.198>.
- [9] W. Huo, X. Liu, S. Tan, F. Fang, Z.H. Xie, J.K. Shang, J.Q. Jiang, Ultrahigh hardness and high electrical resistivity in nano-twinned, nanocrystalline high-entropy alloy films, *Appl. Surf. Sci.* 439 (2018) 222–225, <https://doi.org/10.1016/j.apsusc.2018.01.050>.
- [10] S. Zheng, Z. Cai, J. Pu, C. Zeng, L. Wang, Passivation behavior of VAI TiCrSi amorphous high entropy alloy film with a high corrosion-resistance in artificial sea water, *Appl. Surf. Sci.* 542 (2021), 148520, <https://doi.org/10.1016/j.apsusc.2020.148520>.
- [11] M. Gueye, S. Ammar-Merah, S. Nowak, P. Decorse, A. Chevillot-Biraud, L. Perriere, J.P. Couzinie, I. Guillot, G. Dirras, Study of the stability under in vitro physiological conditions of surface silanated equimolar HfNbTaTiZr high-entropy alloy: a first step toward bio-implant applications, *Surf. Coat. Technol.* 385 (2020), 125374, <https://doi.org/10.1016/j.surfcoat.2020.125374>.
- [12] N.S. Peighambarioust, A.A. Alamdar, U. Unal, A. Motallebzadeh, In vitro biocompatibility evaluation of Ti1.5ZrTa0.5Nb0.5Hf0.5 refractory high-entropy alloy film for orthopedic implants: microstructural, mechanical properties and corrosion behavior, *J. Alloys Compd.* 883 (2021), 160786, <https://doi.org/10.1016/j.jallcom.2021.160786>.
- [13] D.W. Luo, Q. Zhou, W.T. Ye, Y. Ren, C.T. Greiner, Y.X. He, H.F. Wang, Design and characterization of self-lubricating refractory high entropy alloy-based multilayered films, *ACS Appl. Mater. Interfaces* 13 (46) (2021) 55712–55725, <https://doi.org/10.1021/acsami.1c16949>.
- [14] J.A. Smeltzer, B.C. Hornbuckle, A.K. Giri, Nitrogen-induced hardening of refractory high entropy alloys containing laminar ordered phases, *Acta Mater.* 211 (46) (2021), 116884, <https://doi.org/10.1016/j.actamat.2021.116884>.
- [15] S. Lv, Y. Zu, G. Chen, B. Zhao, W. Zhou, A multiple nonmetallic atoms co-doped CrMoNbWTi refractory high-entropy alloy with ultra-high strength and hardness, *Mater. Sci. Eng. A* 795 (2020), 140035, <https://doi.org/10.1016/j.msea.2020.140035>.
- [16] U. Jansson, E. Lewin, Sputter deposition of transition-metal carbide films - a critical review from a chemical perspective, *Thin Solid Films* 536 (1) (2013) 1–24, <https://doi.org/10.1016/j.tsf.2013.02.019>.
- [17] Y.J. Chen, X.H. An, Z.F. Zhou, J.S. Ma, P. Munroe, S. Zhang, Z. Xie, Remarkable toughness of a nanostructured medium-entropy nitride compound, *Nanoscale* 13 (35) (2021) 15074–15084, <https://doi.org/10.1039/DINR03289E>.
- [18] V. Braic, M. Balaceanu, M. Braic, A. Vladescu, S. Panseri, A. Russo, Characterization of multi-principal-element (TiZrNbHfTa)N and (TiZrNbHfTa)C coatings for biomedical applications, *J. Mech. Behav. Biomed.* 10 (2012) 197–205, <https://doi.org/10.1016/j.jmbbm.2012.02.020>.
- [19] S. Alvi, D.M. Jarzabek, M.G. Kohan, D. Hedman, F. Akhtar, Synthesis and mechanical characterization of a CuMoTaWV high-entropy film by magnetron sputtering, *ACS Appl. Mater. Interfaces* 12 (18) (2020) 21070–21079, <https://doi.org/10.1021/acsami.0c02156>.
- [20] B.R. Braeckman, F. Misják, G. Radnócz, M. Caplovicová, D. Depla, The nanostructure and mechanical properties of nanocomposite Nb_x-CoCrCuFeNi thin films, *Scripta Mater.* 139 (2017) 155–158, <https://doi.org/10.1016/j.scriptamat.2017.06.046>.
- [21] B.E. MacDonald, Z. Fu, B. Zheng, W. Chen, Y. Lin, F. Chen, L. Zhang, J. Ivanisenko, Y. Zhou, H. Hahn, E.J. Lavernia, Recent progress in high entropy alloy research, *JOM* 69 (2017) 2024–2031, <https://doi.org/10.4028/www.scientific.net/AMR.63.1-632.227>.
- [22] W. Zhang, Y. Zhang, Science and technology in high-entropy alloys, *Sci. China Mater.* (2018) 2–22, <https://doi.org/10.1007/s40843-017-9195-8>.
- [23] Y. Cheng, Y.F. Zheng, Characterization of TiN, TiC and TiCN coatings on Ti-50.6 at. % Ni alloy deposited by PIII and deposition technique, *Surf. Coat. Technol.* 201 (9–11) (2007) 4909–4912, <https://doi.org/10.1016/j.surfcoat.2006.07.216>.
- [24] R. Chen, J.P. Tu, D.G. Liu, Y.J. Mai, C.D. Gu, Microstructure, mechanical and tribological properties of TiCN nanocomposite films deposited by DC magnetron sputtering, *Surf. Coat. Technol.* 205 (21–22) (2011) 5228–5234, <https://doi.org/10.1016/j.surfcoat.2011.05.034>.
- [25] P. Hu, B. Jiang, Study on tribological property of CrCN coating based on magnetron sputtering plating technique, *Vacuum* 85 (11) (2011) 994–998, <https://doi.org/10.1016/j.vacuum.2011.02.007>.
- [26] Y. Wang, J. Zhang, S. Zhou, Y. Wang, Q. Xue, Improvement in the tribocorrosion performance of CrCN coating by multilayered design for marine protective application, *Appl. Surf. Sci.* 528 (2020), 147061, <https://doi.org/10.1016/j.apsusc.2020.147061>.
- [27] H. Du, P. Liu, W. Li, K. Zhang, P.K. Liaw, Effects of C/Si ratios on structures and behaviors of NbSiCN nanocomposite films synthesized by reactive magnetron sputtering, *Mater. Char.* 167 (2020), 110466, <https://doi.org/10.1016/j.matchar.2020.110466>.
- [28] Y.F. Qin, G.F. Zhu, L.Y. He, J. Zhang, F.Y. Dong, Y.C. Yin, F. Xing, Structure and wear characteristics of TiCN nanocomposite coatings fabricated by reactive plasma spraying, *Surf. Coat. Technol.* 342 (2018) 137–145, <https://doi.org/10.1016/j.surfcoat.2018.02.108>.
- [29] A. Leyland, A. Matthews, On the significance of the H/E ratio in wear control: a nanocomposite coating approach to optimised tribological behaviour, *Wear* 246 (1–2) (2000) 1–11, [https://doi.org/10.1016/s0043-1648\(00\)00488-9](https://doi.org/10.1016/s0043-1648(00)00488-9).
- [30] P.H. Mayrhofer, C. Mitterer, J. Musil, Structure–property relationships in single- and dual-phase nanocrystalline hard coatings, *Surf. Coat. Technol.* 174 (none) (2003) 725–731, [https://doi.org/10.1016/S0257-8972\(03\)00576-0](https://doi.org/10.1016/S0257-8972(03)00576-0).
- [31] X. Xu, J.F. Sun, Z.B. Xu, Z.J. Li, F.H. Su, Microstructure, electrochemical and tribocorrosion behaviors of CrCN nanocomposite coating with various carbon content, *Surf. Coat. Technol.* 411 (2021), 126997, <https://doi.org/10.1016/j.surfcoat.2021.126997>.
- [32] L. Aissani, A. Alhussein, A. Belgroune, C. Nouveau, E. Zghib, R. Barille, A. Montagne, Effect of carbon content on structural, mechanical and tribological properties of Cr-V-C-N coatings, *Thin Solid Films* 732 (2021), 138782, <https://doi.org/10.1016/j.tsf.2021.138782>.
- [33] H. Sun, A. Billard, H. Luo, W.T. Zheng, F. Sanchez, Influence of carbon content on the mechanical properties of TiCN-Cu nanocomposite coatings prepared by multi-arc ion plating, *Vacuum* 187 (2021), 110139, <https://doi.org/10.1016/j.vacuum.2021.110139>.
- [34] J.M. Wu, S.J. Lin, J.W. Yeh, S.K. Chen, H.C. Chen, Adhesive wear behavior of AlxCoCrCuFeNi high-entropy alloys as a function of aluminum content, *Wear* 261 (5–6) (2006) 513–519, <https://doi.org/10.1016/j.wear.2005.12.008>.
- [35] Z.M. Guo, Z.M. Zhang, A.J. Han, J.S. Meng, J. Hu, Microstructure, mechanical and tribological properties of CoCrFeNiMn high entropy alloy matrix composites with addition of Cr3C2, *Tribol. Int.* 151 (2020), 106436, <https://doi.org/10.1016/j.triboint.2020.106436>.
- [36] Z. Cai, Z. Wang, Y. Hong, B. Lu, J. Liu, Y. Li, J. Pu, Improved tribological behavior of plasma-nitrided AlCrTiV and AlCrTiVSi high-entropy alloy films, *Tribol. Int.* 163 (2021), 107195, <https://doi.org/10.1016/j.triboint.2021.107195>.
- [37] V. Bhardwaj, Q. Zhou, F. Zhang, W. Han, H. Wang, Effect of Al addition on the microstructure, mechanical and wear properties of TiZrNbHf refractory high entropy alloys, *Tribol. Int.* 160 (2021), 107031, <https://doi.org/10.1016/j.triboint.2021.107031>.